C. R. Physique 16 (2015) 776–788

Contents lists available at ScienceDirect

Comptes Rendus Physique

www.sciencedirect.com

Radio science for connecting humans with information systems / L'homme connecté

A regularised boundary element formulation for contactless SAR evaluations within homogeneous and inhomogeneous head phantoms

Une formulation aux éléments de frontière régularisée pour l'évaluation sans contact du DAS dans des fantômes de tête homogènes et inhomogènes

Rajendra Mitharwal, Francesco P. Andriulli

Computational Electromagnetics Research Laboratory, Microwave Department, Télécom Bretagne, Brest, France

A R T I C L E I N F O

Article history:
Available online 10 November 2015

Keywords:
Computational dosimetry
SAR assessments
Boundary Element Method
Calderón preconditioning

Mots-clés :
Dosimétrie computationnelle
Evaluations SAR
Méthode des élements de frontière
Préconditionnement de Calderón

A B S T R A C T

This work presents a Boundary Element Method (BEM) formulation for contactless electromagnetic field assessments. The new scheme is based on a regularised BEM approach that requires the use of electric measurements only. The regularisation is obtained by leveraging on an extension of Calderón techniques to rectangular systems leading to well-conditioned problems independent of the discretisation density. This enables the use of highly discretized Huygens surfaces that can be consequently placed very near to the radiating source. In addition, the new regularised scheme is hybridised with both surfacic homogeneous and volumetric inhomogeneous forward BEM solvers accelerated with fast matrix–vector multiplication schemes. This allows for rapid and effective dosimetric assessments and permits the use of inhomogeneous and realistic head phantoms. Numerical results corroborate the theory and confirms the practical effectiveness of all newly proposed formulations.

R É S U M É

Cet article présente une méthode aux éléments de frontière (BEM) adaptée à l'évaluation sans contact du champ électromagnétique. La nouvelle approche est fondée sur une formulation intégrale régularisée, qui nécessite seulement des mesures du champ électrique. La régularisation est obtenue à partir d'une extension des techniques de préconditionnement de type Calderón aux matrices rectangulaires. Cela résulte en des systèmes bien conditionnés indépendamment de la densité de discrétisation et permet l'utilisation de surfaces de Huygens ayant une discrétisation très fine qui, par voie de conséquence, peuvent être placées très près de la source rayonnante. En outre, la nouvelle formulation est hybridée avec deux solveurs d'intégrales de surface (pour des problèmes homogènes) et de volume (pour des problèmes non homogènes) et est accélérée avec des algorithmes rapides de multiplication matrice–vecteur. Ceci permet des évaluations dosimétriques rapides et efficaces et permet aussi l'utilisation de fantômes de tête non homogènes et

E-mail address: francesco.andriulli@telecom-bretagne.eu (F.P. Andriulli).

http://dx.doi.org/10.1016/j.crhy.2015.10.003
1631-0705/

réalistes. Les résultats numériques corroborent la théorie et confirment l'efficacité pratique de toutes les nouvelles formulations proposées.

1. Introduction

Cellular phones, laptops, bluetooth/wireless hotspots, broadcasting systems are all devices that emit mid-to-high doses of electromagnetic radiation that penetrates materials and biological tissues in their vicinities. Recommendations from various institutions in Europe and United States, dictate strict limits on the amount of electromagnetic radiation that can be tolerated within tissues and anatomical parts surrounding a radiating source. The guidelines from the International Commission on Non-Ionizing Radiation Protection (ICNIRP), that are the legal standard in Europe [1,2], are dictating restrictions in terms of electric field induced in tissues (frequency range up to 100 kHz [3,4]), specific absorption rate (SAR, frequency range 100 kHz–10 GHz [5]), and incident power density (frequency range 10 GHz–300 GHz [5]). The early validation against these limits is a crucial step in every industrial process involving radiating elements in the design.

Common technologies and standards that industry uses to assess the electromagnetic exposure and field levels are largely based on internal probes [6] and phantoms [6–8]. Phantoms are suitably designed dielectric structures obtained by filling with a dissipative liquid a container mimicking the shape of different anatomical parts whose electromagnetic exposition needs to be studied [9,10]. The measuring probes penetrate the phantom and effectuate measures of the electric and/or magnetic field [11,12]. Unfortunately however, such an invasive measurement procedure presents several drawbacks. It is costly, since it necessitates ad-hoc mechanical set-ups. It does not guarantee a perturbation-free measurement since an internal probing can perturb the value of the measured fields [13,14]. Finally, it has the need of repeatedly penetrating the dielectric phantom, something that prevents the use of solid dielectric materials and, as a consequence, liquid filled phantoms provide homogeneous and isotropic dielectric profiles only. This is a poor and unrealistic modelling of biological tissues whose dielectric/resistive properties are often both inhomogeneous and anisotropic [15–18].

A first class of partial solutions to some of the above-mentioned issues relies on techniques for determining optimal sets of measurement samples. This for the purpose of reducing the overall number of measurements that are necessary for a full characterisation of the radiation exposure [19–22]. Although these techniques decrease the complexity of a standard, phantom-based, electromagnetic exposure analysis, they are still very complicated to implement, and they leave the modelling limitations of the phantom/probe approach, lamentably, unaltered. A second and more recent class of enhanced dosimetry assessment techniques relies on the use of computational imaging tools to complement the raw measurements of the electromagnetic field. Under this category fall several schemes that adopt finite element based discretisations of models of human tissues and, given an external measurements of the electromagnetic field, solve the electromagnetic problem by using FDTD [23–25], FEM [26–28], and related methods [29–33]. Although effective and easily available from commercial simulation toolboxes, these schemes often rely on a good knowledge of radiation sources, something that is often unavailable in dosimetry assessment.

An effective remedy to these issues is proposed by methods relying on the use of the Huygens principle [34,35], where the (potentially unknown) source is replaced by a surfacic distribution of equivalent sources that are determined together with the field values necessary for the dosimetric assessment. These strategies however, often require the use of densely discretized Huygens surfaces and, when differential equation based methods are the leading modelling formulation, CFL conditions and low-frequency issues (see [36] and references therein) may render the approach computationally expensive. A good alternative could be the use of Huygens principle formulations based on Boundary Element Methods (BEMs). These approaches discretise only material boundaries and are not subject to CFL constraints so that an increase of discretisation density in some parts of the Huygens screen would not result in increase in other parts of the simulation volume. Very promising formulations following these strategies have been presented in [37–39]. These schemes encompass the model of a dosimetric phantom with an equivalent surface and establish a suitable integral relationship linking equivalent sources with magnetic and electric field measurements. Such a strategy falls in the more general category of inverse source approaches that have been studied extensively in the electromagnetic characterisation of radiating sources [40–45]. The problem of characterising the sources, especially in the presence of severe ill-posedness has also been impacted by more general techniques in inverse scattering and imaging where the regularisation techniques of inverse problems related to imaging have been adapted to microwave imaging for human body tissues and their anomalies [46–53].

Integral equation techniques however, are not panacea; BEM methods in fact suffer from a major drawback viz. they give rise to dense interaction matrices, resulting in high computational costs when realistic modelling are called for. Moreover, classical formulations rely often on Dirichlet-to-Neumann mappings (linking magnetic to electric field quantities and vice-versa) that are well-known to be ill-posed and unbounded operators [54]. For this reason although the use of dense equivalent surfaces does not impact a volume discretisation (as in CFL prone methods) it still gives rise to ill-conditioned system as a function of the discretisation density that can result in high computational costs for the solution and in numerical instabilities in real case scenarios.

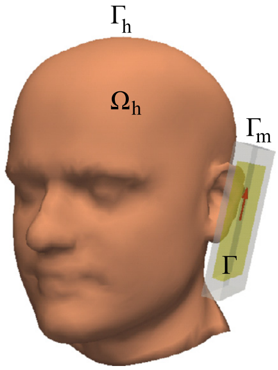

Fig. 1. (Colour online.) Volume and surface definitions.

This work focuses in addressing these drawbacks and its contribution is threefold: (i) It will propose a BEM based formulation that requires the use of electric measurements only. This is done at the cost of solving an additional integral problem with respect to the works in [37], but it has the practical advantage of avoiding magnetic field measurements and the theoretical advantage of providing more freedom in the choice of the mapping operators and in the integral formulation modelling the dosimetric phantom. (ii) This additional freedom will be exploited to use a Huygens formulation that can be regularised. For this purpose this work will propose a Calderón-based strategy for rectangular matrices that will provide well-conditioned systems independent on the discretisation density of the Huygens screen. (iii) Finally, we will hybridise our formulation with both surfacic homogeneous and volumetric inhomogeneous forward BEM solvers accelerated with fast matrix–vector multiplication schemes. This allows for rapid and effective dosimetric assessments and it permits the use of inhomogeneous and realistic head phantoms.

This paper is organised as follows: Section 2 presents background material and sets the notation. Section 3 presents the Huygens formulation we are adopting here. Section 4 presents a Calderón regularisation for rectangular matrices. Section 5 presents numerical results that confirms the practical effectiveness of the new approaches. Section 6 presents our conclusions and avenues for future work.

2. Background and notation

Consider a volume Ω_h (please refer to Fig. 1) characterised by a (potentially lossy and inhomogeneous) dielectric permittivity $\epsilon_h(\boldsymbol{r})$ and residing in a free-space of dielectric permittivity and magnetic permeability ϵ and μ, respectively. The surface of Ω_h is denoted as $\Gamma_h = \partial\Omega_h$. Consider a (potentially unknown) source radiating the electromagnetic field $\left(\boldsymbol{E}^i(\boldsymbol{r}), \boldsymbol{H}^i(\boldsymbol{r})\right)$; the source resides in the interior of the closed surface Γ (an equivalent, Huygens, surface). The total electric field $\boldsymbol{E}(\boldsymbol{r})$ is assumed to be known on a surface Γ_m as a result of a measurement procedure. In our application scenario, Ω_h will model a (potentially lossy and inhomogeneous) head phantom while the source, entirely included in the closed surface Γ, will model a mobile phone radiator (the model of which is potentially unknown).

On the equivalent surface Γ we can define the following surface operators

$$\mathcal{S}^k_\Gamma(\boldsymbol{f}(\boldsymbol{r})) = \mathrm{i}k\int_\Gamma \frac{\mathrm{e}^{\mathrm{i}k|\boldsymbol{r}-\boldsymbol{r}'|}}{4\pi|\boldsymbol{r}-\boldsymbol{r}'|}\boldsymbol{f}(\boldsymbol{r}')\,\mathrm{d}\Gamma - \frac{1}{\mathrm{i}k}\nabla\int_\Gamma \frac{\mathrm{e}^{\mathrm{i}k|\boldsymbol{r}-\boldsymbol{r}'|}}{4\pi|\boldsymbol{r}-\boldsymbol{r}'|}\nabla'\cdot\boldsymbol{f}(\boldsymbol{r}')\,\mathrm{d}\Gamma \tag{1}$$

$$\mathcal{D}^k_\Gamma(\boldsymbol{f}(\boldsymbol{r})) = -\int_\Gamma \nabla\frac{\mathrm{e}^{\mathrm{i}k|\boldsymbol{r}-\boldsymbol{r}'|}}{4\pi|\boldsymbol{r}-\boldsymbol{r}'|}\times\boldsymbol{f}(\boldsymbol{r}')\,\mathrm{d}\Gamma \tag{2}$$

where k is the free space wave number.

When the dielectric profile of Ω_h is homogeneous, i.e. $\epsilon_h(\boldsymbol{r}) = \epsilon_h$, we denote with k_h the associated wave number in Ω_h. In this case, with identical definitions with respect to the ones in (1) and (2), we define the operators $\mathcal{S}^k_{\Gamma_h}$, $\mathcal{D}^k_{\Gamma_h}$ and $\mathcal{S}^{k_h}_{\Gamma_h}$, $\mathcal{D}^{k_h}_{\Gamma_h}$ for which the integrals are defined on the surface Γ_h and for which the wave numbers are set equal to k and k_h, respectively. In the following we will also need the definition of the surface operators $\mathcal{T}^k_{\Gamma_h} = \hat{\boldsymbol{n}}\times\mathcal{S}^k_{\Gamma_h}$, $\mathcal{T}^{k_h}_{\Gamma_h} = \hat{\boldsymbol{n}}\times\mathcal{S}^{k_h}_{\Gamma_h}$, $\mathcal{K}^k_{\Gamma_h} = \hat{\boldsymbol{n}}\times\mathcal{D}^{k_h}_{\Gamma_h}$ and $\mathcal{K}^{k_h}_{\Gamma_h} = \hat{\boldsymbol{n}}\times\mathcal{D}^{k_h}_{\Gamma_h}$ for an outward directed normal $\hat{\boldsymbol{n}}$ on the surface Γ_h and the definition of the free space and relative wave impedance $\eta = \sqrt{\mu/\epsilon}$ and $\eta_r = k/k_h$, respectively.

When the dielectric profile of Ω_h is inhomogeneous, i.e. for general, potentially position-dependent, $\epsilon_h(\boldsymbol{r})$, we define the dielectric contrast ratio as $\chi(\boldsymbol{r}) = 1 - \frac{\epsilon_h(\boldsymbol{r})}{\epsilon}$. In this case, we define the volume operator

$$\mathcal{S}^{k}_{\Omega_h}(\boldsymbol{f}(\boldsymbol{r})) = \mathrm{i}k \int_{\Omega_h} \frac{\mathrm{e}^{\mathrm{i}k|\boldsymbol{r}-\boldsymbol{r}'|}}{4\pi|\boldsymbol{r}-\boldsymbol{r}'|}(\chi(\boldsymbol{r}')\boldsymbol{f}(\boldsymbol{r}'))\,\mathrm{d}\Omega - \frac{1}{\mathrm{i}k}\nabla \int_{\Omega_h} \frac{\mathrm{e}^{\mathrm{i}k|\boldsymbol{r}-\boldsymbol{r}'|}}{4\pi|\boldsymbol{r}-\boldsymbol{r}'|}\nabla'\cdot(\chi(\boldsymbol{r}')\boldsymbol{f}(\boldsymbol{r}'))\,\mathrm{d}\Omega \tag{3}$$

3. The inverse source scheme

It is very well known from potential theory [55] that we can represent the field radiated *outside* Γ from sources located *inside* Γ as

$$\boldsymbol{E}_{\text{ext}}(\boldsymbol{r}) = \alpha\mathcal{S}^{k}_{\Gamma}(\boldsymbol{J}(\boldsymbol{r}',\alpha,\beta)) + \beta\mathcal{D}^{k}_{\Gamma}(\boldsymbol{M}(\boldsymbol{r}',\alpha,\beta)) \tag{4}$$

and

$$\eta\boldsymbol{H}_{\text{ext}} = \frac{1}{\mathrm{i}k}\nabla\times\boldsymbol{E}_{\text{ext}}(\boldsymbol{r}) \tag{5}$$

where α and β can be arbitrarily chosen. The values of $\boldsymbol{J}(\boldsymbol{r}')$ and $\boldsymbol{M}(\boldsymbol{r}')$ will be a function of this arbitrary choice while the resulting value of $\boldsymbol{E}_{\text{ext}}(\boldsymbol{r})$ will be independent of it. A common choice is $\alpha = \beta = 1$, for which $\boldsymbol{J}(\boldsymbol{r}')$ and $\boldsymbol{M}(\boldsymbol{r}')$ have the particularly physical meaning of being the Love's currents [56] equal to $\hat{\boldsymbol{n}}_{\boldsymbol{r}}\times\boldsymbol{H}_{\text{ext}}(\boldsymbol{r})$ and $-\hat{\boldsymbol{n}}_{\boldsymbol{r}}\times\boldsymbol{E}_{\text{ext}}(\boldsymbol{r})$ respectively ($\hat{\boldsymbol{n}}_{\boldsymbol{r}}$ represents the outward directed normal on Γ). Given that we want to avoid the measurement of the magnetic field, however, this choice does not suit our treatment. We select instead $\alpha = 1$ and $\beta = 0$, in this case we deal only with the current distribution $\boldsymbol{J}(\boldsymbol{r}')$ that in the general case however, does not have a straightforward physical interpretation. We thus *define* $\boldsymbol{J}(\boldsymbol{r}')$ the (unknown) current distribution on Γ such that

$$\boldsymbol{E}_{\text{ext}}(\boldsymbol{r}) = \mathcal{S}^{k}_{\Gamma}(\boldsymbol{J}(\boldsymbol{r}')) \tag{6}$$

and

$$\eta\boldsymbol{H}_{\text{ext}}(\boldsymbol{r}) = \frac{1}{\mathrm{i}k}\nabla\times\mathcal{S}^{k}_{\Gamma}(\boldsymbol{J}(\boldsymbol{r}')) \tag{7}$$

$\forall\boldsymbol{r}\in\mathbb{R}^3/\Omega$. The reader should again notice that the current $\boldsymbol{J}(\boldsymbol{r}')$ will not be a simple function of the tangential component of the total magnetic field, like the standard electric current is, but it will be a more complicated function of tangential components of both total electric and magnetic fields. Given however that the radiated fields are to be recovered only in the external region of the equivalent surface, the complicated relationship between the current and the total fields will never be used nor required to be made explicit.

3.1. Homogeneous head model

We assume in this section that the dielectric profile of the head is homogeneous in Ω_h. The purpose of the dosimetric assessment is to find the value of $\boldsymbol{E}(\boldsymbol{r})$, $\boldsymbol{r}\in\Omega_h$, i.e. the total electric field within the head. This field is computed using the surface currents on the surface Γ_h. These unknown surface currents on the head due to the external field radiated by the equivalent current $\boldsymbol{J}(\boldsymbol{r})$, given the homogeneity of the dielectric profile on Γ_h can be obtained by solving the PMCHWT integral equation given by

$$\begin{bmatrix} (\mathcal{T}^{k}_{\Gamma_h}+\mathcal{T}^{k_h}_{\Gamma_h}/\eta_r) & -(\mathcal{K}^{k}_{\Gamma_h}+\mathcal{K}^{k_h}_{\Gamma_h}) \\ (\mathcal{K}^{k}_{\Gamma_h}+\mathcal{K}^{k_h}_{\Gamma_h}) & (\mathcal{T}^{k}_{\Gamma_h}+\eta_r\mathcal{T}^{k_h}_{\Gamma_h}) \end{bmatrix} \begin{bmatrix} \boldsymbol{M}_h(\boldsymbol{r}') \\ \boldsymbol{J}_h(\boldsymbol{r}') \end{bmatrix} = \begin{bmatrix} -\hat{\boldsymbol{n}}\times\eta\boldsymbol{H}_{\text{ext}}(\boldsymbol{r}) \\ -\hat{\boldsymbol{n}}\times\boldsymbol{E}_{\text{ext}}(\boldsymbol{r}) \end{bmatrix} \tag{8}$$

where the unknown electric and magnetic surface currents denoted by $\boldsymbol{J}_h(\boldsymbol{r}')$ and $\boldsymbol{M}_h(\boldsymbol{r}')$ for $\boldsymbol{r}'\in\Gamma_h$ respectively can be found using

$$\begin{bmatrix} \boldsymbol{M}_h(\boldsymbol{r}') \\ \boldsymbol{J}_h(\boldsymbol{r}') \end{bmatrix} = \begin{bmatrix} (\mathcal{T}^{k}_{\Gamma_h}+\mathcal{T}^{k_h}_{\Gamma_h}/\eta_r) & -(\mathcal{K}^{k}_{\Gamma_h}+\mathcal{K}^{k_h}_{\Gamma_h}) \\ (\mathcal{K}^{k}_{\Gamma_h}+\mathcal{K}^{k_h}_{\Gamma_h}) & (\mathcal{T}^{k}_{\Gamma_h}+\eta_r\mathcal{T}^{k_h}_{\Gamma_h}) \end{bmatrix}^{-1} \begin{bmatrix} -\hat{\boldsymbol{n}}\times\eta\boldsymbol{H}_{\text{ext}}(\boldsymbol{r}) \\ -\hat{\boldsymbol{n}}\times\boldsymbol{E}_{\text{ext}}(\boldsymbol{r}) \end{bmatrix} \tag{9}$$

and from which the field $\boldsymbol{E}_h(\boldsymbol{r})$ scattered by the head can be obtained as

$$\boldsymbol{E}_h(\boldsymbol{r}) = \mathcal{S}^{k}_{\Gamma_h}(\boldsymbol{J}_h(\boldsymbol{r}')) + \mathcal{D}^{k}_{\Gamma_h}(\boldsymbol{M}_h(\boldsymbol{r}')) \quad \boldsymbol{r}\in\mathbb{R}^3/\Omega_h \tag{10}$$

or

$$\boldsymbol{E}_h(\boldsymbol{r}) = [\,\mathcal{D}^{k}_{\Gamma_h} \quad \mathcal{S}^{k}_{\Gamma_h}\,] \begin{bmatrix} (\mathcal{T}^{k}_{\Gamma_h}+\mathcal{T}^{k_h}_{\Gamma_h}/\eta_r) & -(\mathcal{K}^{k}_{\Gamma_h}+\mathcal{K}^{k_h}_{\Gamma_h}) \\ (\mathcal{K}^{k}_{\Gamma_h}+\mathcal{K}^{k_h}_{\Gamma_h}) & (\mathcal{T}^{k}_{\Gamma_h}+\eta_r\mathcal{T}^{k_h}_{\Gamma_h}) \end{bmatrix}^{-1} \begin{bmatrix} -\hat{\boldsymbol{n}}\times\eta\boldsymbol{H}_{\text{ext}}(\boldsymbol{r}) \\ -\hat{\boldsymbol{n}}\times\boldsymbol{E}_{\text{ext}}(\boldsymbol{r}) \end{bmatrix} \tag{11}$$

This can be further written as a function of $\boldsymbol{J}(\boldsymbol{r}')$ on Γ by leveraging on (6) and (7) as

$$\boldsymbol{E}_h(\boldsymbol{r}) = [\,\mathcal{D}^k_{\Gamma_h} \quad \mathcal{S}^k_{\Gamma_h}\,]\begin{bmatrix} (\mathcal{T}^k_{\Gamma_h} + \mathcal{T}^{k_h}_{\Gamma_h}/\eta_r) & -(\mathcal{K}^k_{\Gamma_h} + \mathcal{K}^{k_h}_{\Gamma_h}) \\ (\mathcal{K}^k_{\Gamma_h} + \mathcal{K}^{k_h}_{\Gamma_h}) & (\mathcal{T}^k_{\Gamma_h} + \eta_r \mathcal{T}^{k_h}_{\Gamma_h}) \end{bmatrix}^{-1} \cdot \begin{bmatrix} -\hat{\boldsymbol{n}} \times \eta \frac{1}{ik} \nabla \times \mathcal{S}^k_{\Gamma}(\boldsymbol{J}(\boldsymbol{r}')) \\ -\hat{\boldsymbol{n}} \times \mathcal{S}^k_{\Gamma}(\boldsymbol{J}(\boldsymbol{r}')) \end{bmatrix} \tag{12}$$

By enforcing the condition $\boldsymbol{E}(\boldsymbol{r}) = \boldsymbol{E}_{\text{ext}}(\boldsymbol{r}) + \boldsymbol{E}_h(\boldsymbol{r})$ on Γ_m we obtain

$$\mathcal{S}^k_{\Gamma}(\boldsymbol{J}(\boldsymbol{r}')) + [\,\mathcal{D}^k_{\Gamma_h} \quad \mathcal{S}^k_{\Gamma_h}\,]\begin{bmatrix} (\mathcal{T}^k_{\Gamma_h} + \mathcal{T}^{k_h}_{\Gamma_h}/\eta_r) & -(\mathcal{K}^k_{\Gamma_h} + \mathcal{K}^{k_h}_{\Gamma_h}) \\ (\mathcal{K}^k_{\Gamma_h} + \mathcal{K}^{k_h}_{\Gamma_h}) & (\mathcal{T}^k_{\Gamma_h} + \eta_r \mathcal{T}^{k_h}_{\Gamma_h}) \end{bmatrix}^{-1} \cdot \begin{bmatrix} -\hat{\boldsymbol{n}} \times \eta \frac{1}{ik} \nabla \times \mathcal{S}^k_{\Gamma}(\boldsymbol{J}(\boldsymbol{r}')) \\ -\hat{\boldsymbol{n}} \times \mathcal{S}^k_{\Gamma}(\boldsymbol{J}(\boldsymbol{r}')) \end{bmatrix} = \boldsymbol{E}(\boldsymbol{r}), \quad \boldsymbol{r} \in \Gamma_m \tag{13}$$

As pointed out in the previous section, the field $\boldsymbol{E}(\boldsymbol{r})$ is assumed to be known as a result of a measurement procedure, so that the unknown current distribution $\boldsymbol{J}(\boldsymbol{r}')$ can be obtained by inverting (13). This inversion will be obtained by subsequent use of boundary element discretisations as explained in the following section.

As a final remark for this section, we think that the reader may wonder why a single current formulation has been adopted for the Huygens surface and instead a two currents formulation has been adopted on the head surface. The reason behind this choice is that we do not need to calculate the field inside the Huygens surface, but only outside it. In other words we do not need to enforce any transmission conditions on the surface since only the external field is necessary and the current is recovered without the need of recovering the associated values of tangential electric and magnetic fields (for which an additional integral equation should have been solved). Instead, for the dielectric head, we must find the field both outside and inside. For this reason it is more convenient to use a two currents formulation where the transmission conditions are simpler to enforce being only the tangential continuity of the electric and magnetic field.

3.1.1. Discretisation

In order to solve numerically the integral equations defined in the previous section, it is necessary to discretise the involved surface operators. As in any standard boundary element method, we need to approximate the various geometries present with a triangular tessellation giving rise to surface meshes for Γ_h, Γ and Γ_m. On the internal edges of these surface meshes, we can define the sets of Rao–Wilton–Glisson (RWG) basis functions [57] $\{\boldsymbol{f}^h_n\}_{n=1}^{N_h}$, $\{\boldsymbol{f}_n\}_{n=1}^{N}$ and $\{\boldsymbol{f}^m_n\}_{n=1}^{N_m}$ respectively (N_h, N and N_m being the number of edges on Γ_h, Γ and Γ_m respectively). The surface currents can be approximated as

$$\begin{aligned} \boldsymbol{J}_h(\boldsymbol{r}) &= \sum_{n=1}^{N_h} \alpha_n \boldsymbol{f}^h_n(\boldsymbol{r}) \\ \boldsymbol{M}_h(\boldsymbol{r}) &= \sum_{n=1}^{N_h} \beta_n \boldsymbol{f}^h_n(\boldsymbol{r}) \\ \boldsymbol{J}(\boldsymbol{r}) &= \sum_{n=1}^{N} \gamma_n \boldsymbol{f}_n(\boldsymbol{r}) \end{aligned} \tag{14}$$

The different blocks in equation (13) can be discretized as explained in what follows. The PMCHWT operators $\mathcal{T}^k_{\Gamma_h}$, $\mathcal{T}^{k_h}_{\Gamma_h}$, $\mathcal{K}^k_{\Gamma_h}$ and $\mathcal{K}^{k_h}_{\Gamma_h}$ are discretized using the sets of RWG basis functions both as source and testing functions resulting in the matrices

$$\begin{aligned} (\mathbf{T})_{mn} &= \left\langle \hat{\boldsymbol{n}} \times \boldsymbol{f}^h_m(\boldsymbol{r}), \mathcal{T}^k_{\Gamma_h}(\boldsymbol{f}^h_n(\boldsymbol{r}))\right\rangle_{\Gamma_h} \\ (\mathbf{T}')_{mn} &= \left\langle \hat{\boldsymbol{n}} \times \boldsymbol{f}^h_m(\boldsymbol{r}), \mathcal{T}^{k_h}_{\Gamma_h}(\boldsymbol{f}^h_n(\boldsymbol{r}))\right\rangle_{\Gamma_h} \\ (\mathbf{K})_{mn} &= \left\langle \hat{\boldsymbol{n}} \times \boldsymbol{f}^h_m(\boldsymbol{r}), \mathcal{K}^k_{\Gamma_h}(\boldsymbol{f}^h_n(\boldsymbol{r}))\right\rangle_{\Gamma_h} \\ (\mathbf{K}')_{mn} &= \left\langle \hat{\boldsymbol{n}} \times \boldsymbol{f}^h_m(\boldsymbol{r}), \mathcal{K}^{k_h}_{\Gamma_h}(\boldsymbol{f}^h_n(\boldsymbol{r}))\right\rangle_{\Gamma_h} \end{aligned} \tag{15}$$

where the notation $\langle \boldsymbol{a} \cdot \boldsymbol{b} \rangle_\chi = \int_\chi \boldsymbol{a} \cdot \boldsymbol{b} \, d\chi$ and $(\mathbf{A})_{mn}$ represents the element in the row m and the column n of a matrix $\mathbf{A}$. The discretized version of the continuous operators applied to the equivalent source currents radiating the fields on the head surface are given by

$$(\mathbf{K}_\Gamma)_{mn} = \left\langle \hat{\boldsymbol{n}} \times \boldsymbol{f}^h_m(\boldsymbol{r}), -\hat{\boldsymbol{n}} \times \eta_0 \frac{1}{\mathrm{i}k} \nabla \times \mathcal{S}^k_\Gamma(\boldsymbol{f}_n(\boldsymbol{r})) \right\rangle_{\Gamma_h}$$
$$(\mathbf{T}_\Gamma)_{mn} = \left\langle \hat{\boldsymbol{n}} \times \boldsymbol{f}^h_m(\boldsymbol{r}), -\hat{\boldsymbol{n}} \times \mathcal{S}^k_\Gamma(\boldsymbol{f}_n(\boldsymbol{r})) \right\rangle_{\Gamma_h} \tag{16}$$

Similarly, the discretized version of the continuous operators applied to the surface currents on the head radiating the fields on the measurement surface are given by

$$(\mathbf{S}_{\Gamma_h})_{mn} = \left\langle \boldsymbol{f}^m_m(\boldsymbol{r}), \mathcal{S}^k_{\Gamma_h}(\boldsymbol{f}^h_n(\boldsymbol{r})) \right\rangle_\Gamma$$
$$(\mathbf{D}_{\Gamma_h})_{mn} = \left\langle \boldsymbol{f}^m_m(\boldsymbol{r}), \mathcal{D}^k_{\Gamma_h}(\boldsymbol{f}^h_n(\boldsymbol{r})) \right\rangle_\Gamma \tag{17}$$

The incident electric field due to the equivalent source currents on the measurement surface represented as a matrix is given by

$$(\mathbf{S}_\Gamma)_{mn} = \left\langle \boldsymbol{f}^m_m(\boldsymbol{r}), \mathcal{S}^k_\Gamma(\boldsymbol{f}_n(\boldsymbol{r})) \right\rangle_{\Gamma_m} \tag{18}$$

The overall right-hand side vector reads

$$\mathbf{v}_m = \langle \boldsymbol{f}^m_m(\boldsymbol{r}), \boldsymbol{E}(\boldsymbol{r}) \rangle_{\Gamma_m} \tag{19}$$

Finally, define the unknown current coefficients vector

$$(\boldsymbol{\gamma})_m = \gamma_m \tag{20}$$

Leveraging on all the definitions above, the discretisation of equation (13) reads

$$\mathbf{S}_\Gamma \boldsymbol{\gamma} + [\,\mathbf{D}_{\Gamma_h} \quad \mathbf{S}_{\Gamma_h}\,] \begin{bmatrix} (\mathbf{T} + \mathbf{T}'/\eta_r) & -(\mathbf{K} + \mathbf{K}') \\ (\mathbf{K} + \mathbf{K}') & (\mathbf{T} + \eta_r \mathbf{T}') \end{bmatrix}^{-1} \begin{bmatrix} \mathbf{K}_\Gamma \\ \mathbf{T}_\Gamma \end{bmatrix} \boldsymbol{\gamma} = \mathbf{v} \tag{21}$$

3.2. Inhomogeneous head model

In realistic scenarios, the modelling of the human head phantom may result in inhomogeneous dielectric profiles modelling different tissues (typically scalp, skull and brain). The objective of dosimetric assessments remains unchanged from the case analysed in the previous section, i.e. the total electric field inside the head region must be recovered starting from measurements in the vicinities of the radiating source. The total electric field now is the sum of the external field radiated by the equivalent current $\boldsymbol{J}(\boldsymbol{r}')$ and the equivalent volume current $\boldsymbol{J}^v_h(\boldsymbol{r}')$ inside the human head model. The mapping between the volume currents and the external field can be expressed using a Volume Integral Equation (VIE) [58,59]

$$\left[(1 - \chi(\boldsymbol{r}))\frac{\mathcal{I}}{\mathrm{i}k} + \mathcal{S}^k_{\Omega_h}\right] \boldsymbol{J}^v_h(\boldsymbol{r}') = \boldsymbol{E}_{\mathrm{ext}}(\boldsymbol{r}) \quad \boldsymbol{r} \in \Omega_h \tag{22}$$

where $\mathcal{I}$ is the identity operator and the unknown volume current is given by

$$\boldsymbol{J}^v_h(\boldsymbol{r}) = \left[(1 - \chi(\boldsymbol{r}))\frac{\mathcal{I}}{\mathrm{i}k} + \mathcal{S}^k_{\Omega_h}\right]^{-1} \boldsymbol{E}_{\mathrm{ext}}(\boldsymbol{r}') \quad \boldsymbol{r} \in \Omega_h \tag{23}$$

It should be noted that only a volume electric current is necessary since only the electric permittivity is inhomogeneous while the magnetic permeability is perfectly homogeneous ($\mu = \mu_0$). The electric field in the external region due to the volume current inside the head is given by

$$\boldsymbol{E}_h(\boldsymbol{r}) = -\mathcal{S}^k_{\Omega_h} \boldsymbol{J}^v_h(\boldsymbol{r}') \quad \boldsymbol{r} \in \mathbb{R}^3/\Omega_h \tag{24}$$

or

$$\boldsymbol{E}_h(\boldsymbol{r}) = -\mathcal{S}^k_{\Omega_h} \left[(1 - \chi(\boldsymbol{r}))\frac{\mathcal{I}}{\mathrm{i}k} + \mathcal{S}^k_{\Omega_h}\right]^{-1} \boldsymbol{E}_{\mathrm{ext}}(\boldsymbol{r}') \tag{25}$$

which can be written in terms of surface currents on the equivalent surface as

$$\boldsymbol{E}_h(\boldsymbol{r}) = -\mathcal{S}^k_{\Omega_h} \left[(1 - \chi(\boldsymbol{r}))\frac{\mathcal{I}}{\mathrm{i}k} + \mathcal{S}^k_{\Omega_h}\right]^{-1} \mathcal{S}^k_\Gamma(\boldsymbol{J}(\boldsymbol{r}')) \tag{26}$$

The total electric field on the measurement surface Γ_m is thus obtained as

$$\mathcal{S}_{\Gamma}^{k}(\boldsymbol{J}(\boldsymbol{r}')) - \mathcal{S}_{\Omega_h}^{k}\left[(1-\chi(\boldsymbol{r}))\frac{\mathcal{I}}{\mathrm{i}k} + \mathcal{S}_{\Omega_h}^{k}\right]^{-1}\mathcal{S}_{\Gamma}^{k}(\boldsymbol{J}(\boldsymbol{r}')) = \boldsymbol{E}(\boldsymbol{r}) \quad \boldsymbol{r} \in \Gamma_m \tag{27}$$

The above equation gives the relationship between the unknown equivalent surface current and the measured electric field in the presence of an inhomogeneous head model. The unknown surface current $\boldsymbol{J}(\boldsymbol{r}')$ can be obtained by solving the discretized version of the above equation, as explained in the next subsection.

3.2.1. Discretisation

Equation (27) can be discretized after meshing the equivalent surface Γ with triangular cells and the head volume Ω_h with tetrahedral cells. On a pair of triangular cells of the equivalent source and measurement surface, we define the sets of RWG basis functions $\{\boldsymbol{f}_n\}_{n=1}^{N}$ and $\{\boldsymbol{f}_n^m\}_{n=1}^{N_m}$, respectively. Similarly, on a pair of each adjacent tetrahedron of the volume mesh, we define an Schaubert–Wilton–Glisson (SWG) basis function [58] giving rise to the set $\{\boldsymbol{f}_n^v\}_{n=1}^{N_v}$ (N_v represents the number of triangular cells based on which the SWG basis functions are defined). Using these basis functions, we can discretise the volume and surface currents as

$$\begin{aligned}\boldsymbol{J}_v(\boldsymbol{r}) &= \sum_{n=1}^{N_v}\alpha_n \boldsymbol{f}_n^v(\boldsymbol{r})\\ \boldsymbol{J}(\boldsymbol{r}) &= \sum_{n=1}^{N}\gamma_n \boldsymbol{f}_n(\boldsymbol{r})\end{aligned} \tag{28}$$

The VIE operator can be discretized as

$$(\mathbf{S}_{\Omega_h})_{mn} = \left\langle \boldsymbol{f}_m^v(\boldsymbol{r}), \mathcal{S}_{\Omega_h}^{k}(\boldsymbol{f}_n^v(\boldsymbol{r}))\right\rangle_{\Omega_h} \tag{29}$$

and the Gram matrix is given by

$$(\mathbf{G}_{\Omega_h})_{mn} = \left\langle \boldsymbol{f}_m^v(\boldsymbol{r}), \frac{1-\chi(\boldsymbol{r})}{\mathrm{i}k}\boldsymbol{f}_n^v(\boldsymbol{r})\right\rangle_{\Omega_h} \tag{30}$$

The discretized surface operator applied to the equivalent source current radiating on the head surface is given by

$$(\mathbf{S}_{\Gamma}^{\Omega_h})_{mn} = \left\langle \boldsymbol{f}_m^v(\boldsymbol{r}), \mathcal{S}_{\Gamma}^{k}(\boldsymbol{f}_n(\boldsymbol{r}))\right\rangle_{\Omega_h} \tag{31}$$

Similarly, the discretized volume operator applied to the volume currents of the inhomogeneous head model radiating on the measurement surface is given by

$$(\mathbf{S}_{\Omega_h}^{\Gamma})_{mn} = \left\langle \boldsymbol{f}_m^m(\boldsymbol{r}), \mathcal{S}_{\Omega_h}^{k}(\boldsymbol{f}_n^v(\boldsymbol{r}))\right\rangle_{\Gamma_m} \tag{32}$$

The discretisation of the operator defined for the incident electric field due to the equivalent source currents on the measurement surface

$$(\mathbf{S}_{\Gamma})_{mn} = \left\langle \boldsymbol{f}_m^m(\boldsymbol{r}), \mathcal{S}_{\Gamma}^{k}(\boldsymbol{f}_n(\boldsymbol{r}))\right\rangle_{\Gamma_m} \tag{33}$$

and the right-hand side and solution vectors

$$\mathbf{v}_m = \left\langle \boldsymbol{f}_m^m(\boldsymbol{r}), \boldsymbol{E}(\boldsymbol{r})\right\rangle_{\Gamma_m} \tag{34}$$

$$(\boldsymbol{\gamma})_m = \gamma_m \tag{35}$$

remain similar to those of the homogeneous case (treated in the previous section). By combining the discretisations above we obtain the following discretized version of equation (27)

$$\mathbf{S}_{\Gamma}\gamma - \mathbf{S}_{\Omega_h}^{\Gamma}[\mathbf{G}_{\Omega_h} + \mathbf{S}_{\Omega_h}]^{-1}\mathbf{S}_{\Gamma}^{\Omega_h}\gamma = \mathbf{v} \tag{36}$$

4. Calderón preconditioning

As delineated in the previous sections, the linear system of equations (21) and (36) requires near-field measurements for building up the right-hand side vector. A practical case of interest arises when the equivalent surface and the measurement surface coincide, i.e. when $\Gamma_m = \Gamma$. Even in this case, however, the surface meshes on Γ_m and Γ are often different. In fact, the discretisation of the measurement surface is dependent on the overall number of degrees of freedom of the measured near-field values [19,20] and also on the limitations of the measurement system setups [21,60]. On the other hand, the discretisation of the equivalent surface depends on how well it can model the near-field behaviour of the radiating source and it plays a role in the pseudo-inversion procedure. This results in a different discretisation density on the equivalent surface compared to the measurement surface. Therefore, the system matrices in equation (21) and (36) are rectangular and they deal with unequal number of unknowns compared to the number of equations. These equations can be solved in the least squares sense using an iterative solver by applying the transpose to the matrix $\mathbf{S}_\Gamma$ as

$$\mathbf{S}_\Gamma^{\mathrm{T}}[\mathbf{S}_\Gamma + \tilde{\mathbf{S}}_\Gamma]\gamma = \mathbf{S}_\Gamma^{\mathrm{T}}\mathbf{v} \tag{37}$$

where in case of the homogeneous head model

$$\tilde{\mathbf{S}}_\Gamma = [\,\mathbf{D}_{\Gamma_h} \quad \mathbf{S}_{\Gamma_h}\,]\begin{bmatrix} (\mathbf{T}+\mathbf{T}'/\eta_r) & -(\mathbf{K}+\mathbf{K}') \\ (\mathbf{K}+\mathbf{K}') & (\mathbf{T}+\eta_r\mathbf{T}') \end{bmatrix}^{-1}\begin{bmatrix} \mathbf{S}_\Gamma \\ \mathbf{K}_\Gamma \end{bmatrix} \tag{38}$$

and for the inhomogeneous head model

$$\tilde{\mathbf{S}}_\Gamma = -\mathbf{S}_{\Omega_h}^{\Gamma}[\mathbf{G}_{\Omega_h} + \mathbf{S}_{\Omega_h}]^{-1}\mathbf{S}_{\Gamma}^{\Omega_h} \tag{39}$$

In equation (37), the matrix $\tilde{\mathbf{S}}_\Gamma$ represents a compact perturbation of the EFIE operator matrix with a negligible contribution to the spectrum of $\mathbf{S}_\Gamma$. The overall system matrix inherits the ill-conditioning of the EFIE operator due to the dense discretisation and low-frequency breakdown [61]. The condition number of $\mathbf{S}_\Gamma$ shows a behaviour of order $\mathcal{O}(\frac{1}{(kh)^2})$ [62,63]. This results in a conditioning behaviour of order $\mathcal{O}(\frac{1}{(kh)^4})$ for the system matrix $\mathbf{S}_\Gamma^{\mathrm{T}}\mathbf{S}_\Gamma$. Therefore, solving equation (37) becomes a challenging task as the discretisation on the equivalent surface increases and/or the frequency decreases. In this work, we propose to leverage on Calderón preconditioning to solve this problem. Calderón preconditioning is based on the Calderón identity [64,65]

$$(\mathcal{T}_\Gamma^k)^2(\boldsymbol{J}(\boldsymbol{r})) = -\frac{\boldsymbol{J}(\boldsymbol{r})}{4} + (\tilde{\mathcal{K}}_\Gamma^k)^2(\boldsymbol{J}(\boldsymbol{r})) \tag{40}$$

The discretisation of equation (40) results in well conditioned system matrices [64]. The operator $\mathcal{T}_\Gamma^k$ when discretized with the sets of RWG basis functions $\{\boldsymbol{f}_n\}_{n=1}^N$ and $\{\hat{\boldsymbol{n}} \times \boldsymbol{f}_n^m\}_{n=1}^{N_m}$ results in the matrix $\mathbf{S}_\Gamma$. To realise the discretisation of the Calderón identity (equation (40)), however, we also need the sets of Buffa–Christiansen (BC) basis functions $\{\boldsymbol{b}_n\}_{n=1}^N$ and $\{\hat{\boldsymbol{n}} \times \boldsymbol{b}_n^m\}_{n=1}^{N_m}$ (the definition of these functions is omitted here for the sake of brevity, the reader should refer to [66] or [64] for the implementational details of these boundary elements). This discretisation gives rise to the matrix $\mathbf{S}_\Gamma^{BC} = \langle \boldsymbol{b}_m^m(\boldsymbol{r}), \mathcal{S}_\Gamma(\boldsymbol{b}_n(\boldsymbol{r}))\rangle_{\Gamma_m}$. In order to link correctly the basis functions between the two operator matrices $\mathbf{S}_\Gamma^{BC}$ and $\mathbf{S}_\Gamma$, we need a suitable Gram matrix $\mathbf{G}_{\Gamma_m} = \langle \hat{\boldsymbol{n}} \times \boldsymbol{f}_m^m(\boldsymbol{r}), \boldsymbol{b}_n^m(\boldsymbol{r})\rangle_{\Gamma_m}$. The proposed regularised linear system of equations for dosimetry assessment then reads

$$[\mathbf{S}_\Gamma^{BC}]^{\mathrm{T}}[\mathbf{G}_{\Gamma_m}]^{-1}[\mathbf{S}_\Gamma + \tilde{\mathbf{S}}_\Gamma]\boldsymbol{\gamma} = [\mathbf{S}_\Gamma^{BC}]^{\mathrm{T}}[\mathbf{G}_{\Gamma_m}]^{-1}\mathbf{v} \tag{41}$$

5. Numerical results

The first test focused on the validation of the BEM formulation, developed in Section 3.1 for homogeneous phantom profiles. The electric field radiated by a mobile phone antenna in the presence of an homogeneous head phantom is shown in Fig. 2a. The mobile antenna has been enclosed in a parallelepiped's equivalent surface that is also used as measurement surface. After applying the numerical procedure detailed in Section 3.1, the electric field is reconstructed in Fig. 2b. Fig. 4c shows the reconstruction relative error computed as

$$\varepsilon(\boldsymbol{r}) = \frac{|\boldsymbol{E}(\boldsymbol{r}) - \boldsymbol{E}_r(\boldsymbol{r})|}{|\boldsymbol{E}(\boldsymbol{r})|} \tag{42}$$

where the electric field $\boldsymbol{E}(\boldsymbol{r})$ and $\boldsymbol{E}_r(\boldsymbol{r})$ are due to the radiating source and the Huygens surface in the presence of the head, respectively. The maximum field relative error stays below 1%, confirming the validity of the formulation.

A second numerical test has been performed to assess the performance of the BEM formulation, developed in Section 3.2 for inhomogeneous phantom profiles. The inhomogeneous head phantom we have used is shown in Fig. 3. We have adopted an MRI based three layers head model which has a piecewise-constant dielectric profile. The reader should notice, however,

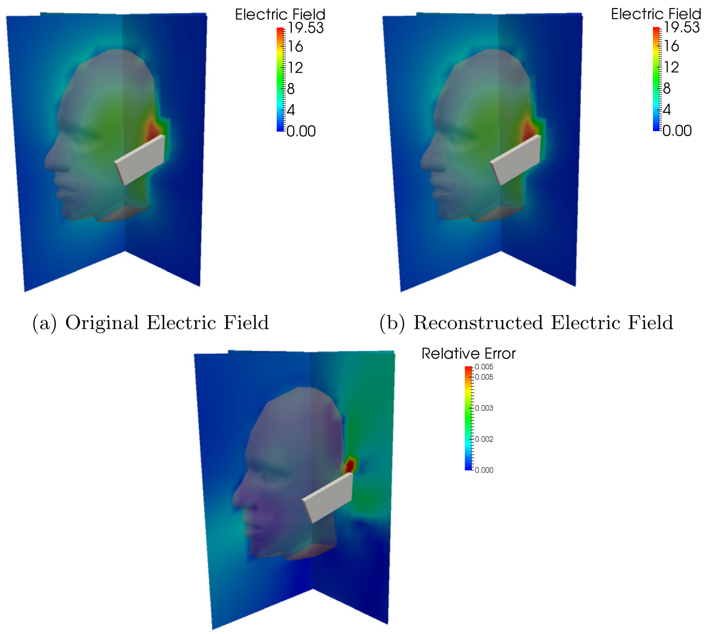

(a) Original Electric Field
(b) Reconstructed Electric Field
(c) Relative Error in Electric Field

Fig. 2. (Colour online.) Homogeneous head model.

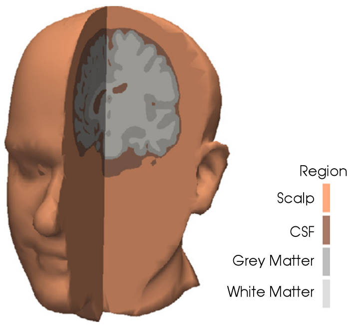

Fig. 3. (Colour online.) Volume regions of the human head model.

that any other dielectric profile of arbitrary inhomogeneity could have been used as well. The electric field radiated by a mobile phone antenna in the presence of this inhomogeneous head phantom is shown in Fig. 4a. The mobile antenna has been again enclosed in a parallelepiped's equivalent surface that is also used as measurement surface. After applying the numerical procedure detailed in Section 3.2, the electric field is reconstructed in Fig. 4b. The reconstruction relative error is shown in Fig. 2c, the maximum field relative error stays well below 1% confirming that also this formulation for inhomogeneous dielectric profiles is a valid one.

A final set of tests has been focused in validating the Calderón regularisations proposed in Section 4. First we have considered two canonical cases (a cube and an hemisphere) to check the stability of the regularisation to mesh refinement. To this purpose the measurement mesh has been kept constant, while the equivalent surface mesh density was increased. For the case of the cube, the condition numbers of the overall system matrix w.r.t. to the average edge length is shown in Fig. 5. It is clear that the regularised system matrix has a constant condition number when the mesh density increases whereas without regularisation a steep condition number growth is observed. A similar behaviour is observed in the case of the hemisphere as it is shown in Fig. 6. The stability of the regularised system with respect to frequency has been tested as well. The condition numbers as a function of the frequency are shown in Fig. 7. Also in this case the regularised formulation is stable, while standard operators show the expected frequency instability. A regularisation in a real case scenario has been equally tested. To this purpose we have used the previous homogeneous head model. The relative tolerance of a CGS solver w.r.t. number of iterations to compute the dosimetry assessment can be seen in Fig. 8. The tolerance curves show that the regularisation proposed here can greatly improve the convergence behaviour and, as a consequence, the time necessary for dosimetric assessment.

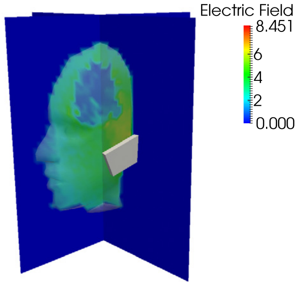

(a) Original Electric Field

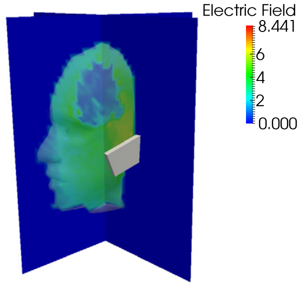

(b) Reconstructed Electric Field

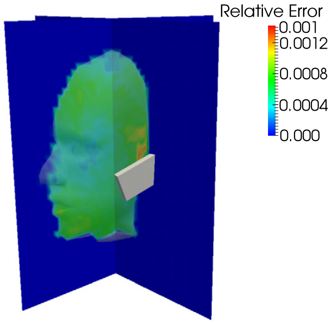

(c) Relative Error in Electric Field

Fig. 4. (Colour online.) Inhomogeneous head model.

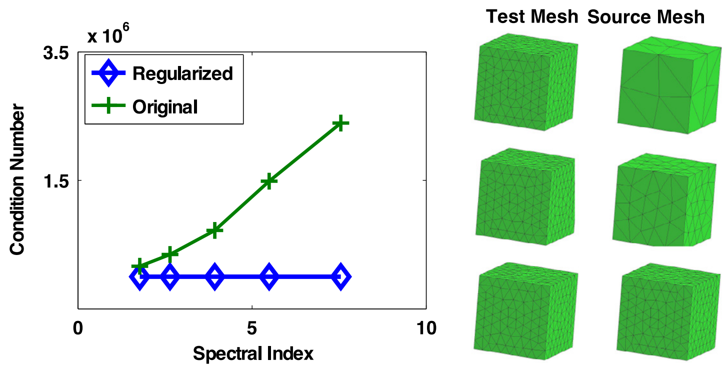

Fig. 5. (Colour online.) Variation of the condition number of a cube mesh.

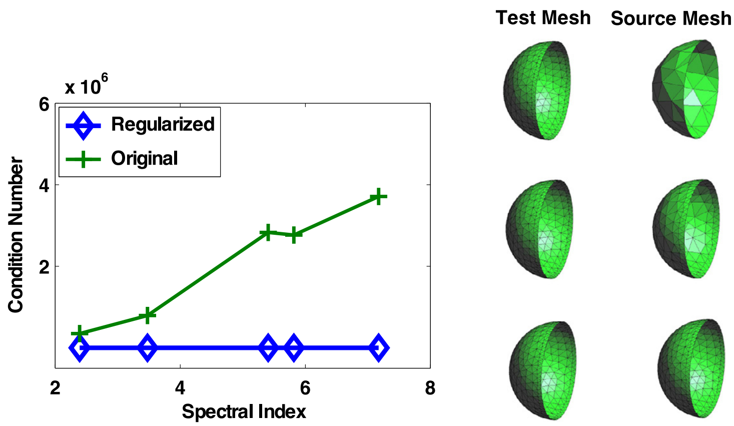

Fig. 6. (Colour online.) Variation of the condition number of a hemisphere mesh.

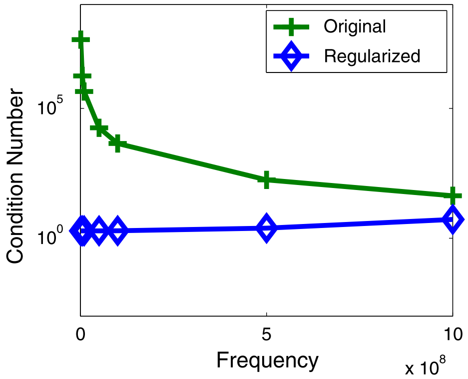

Fig. 7. (Colour online.) Variation of the condition number of a cube mesh w.r.t. frequency.

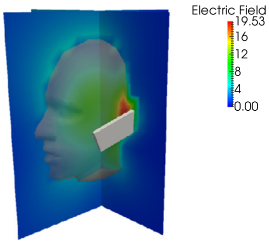

(a) Reconstructed Electric Field

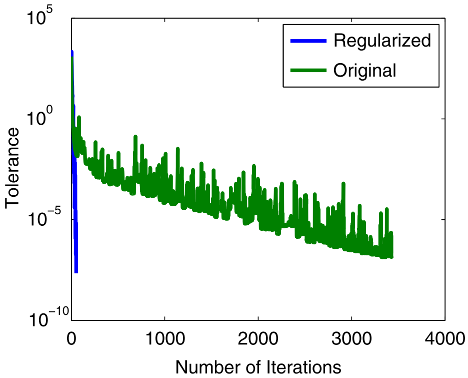

(b) Variation Tolerance Error w.r.t CGS iterations

Fig. 8. (Colour online.) Validation of the Calderón regularisation in a real-case scenario.

6. Conclusions

A Boundary Element Method (BEM) formulation for contactless electromagnetic field assessments has been presented. The new scheme, which is based on a regularised BEM approach, requires the use of electric field measurements only. The regularisation, which is based on Calderón techniques, enables the use of highly discretized Huygens surfaces that can be consequently placed very near to the radiating source. A hybridisation with both surfacic homogeneous and volumetric inhomogeneous forward BEM solvers has been proposed that allows the use of inhomogeneous and realistic head phantoms. Numerical results have been presented that corroborate the theory and confirm the practical effectiveness of all newly proposed formulations. Future investigations will include the extension of the new formulations presented here to the time domain as well as their application to an industrial-level measurement setting.

Acknowledgements

This work was supported in part by the "Agence nationale de la recherche" (France) under Project FASTEEG-ANR-12-JS09-0010, in part by the European Union Marie Curie Project 303750 – NEUROIMAGEEG, in part by the Brittany Region, France, and in part by the HPC resources through the GENCI–TGCC Project under Grant 2015-gen6944.

References

[1] Recommendation Council, 519/EC of 12 July 1999 on the limitation of exposure of the general public to electromagnetic fields (0 Hz to 300 GHz), Off. J. Eur. Communities, L 59 (1999) 59–70.
[2] M. Grandolfo, Worldwide standards on exposure to electromagnetic fields: an overview, The Environmentalist 29 (2) (2009) 109–117.
[3] J. Lin, R. Saunders, K. Schulmeister, P. Söderberg, A. Swerdlow, M. Taki, B. Veyret, G. Ziegelberger, M.H. Repacholi, R. Matthes, et al., ICNIRP guidelines for limiting exposure to time-varying electric and magnetic fields (1 Hz to 100 kHz), Health Phys. 99 (2010) 818–836.
[4] International Commission on Non-Ionizing Radiation Protection and others, Guidance on determining compliance of exposure to pulsed and complex non-sinusoidal waveforms below 100 kHz with ICNIRP guidelines, Health Phys. 84 (3) (2003) 383–387.
[5] International Commission on Non-Ionizing Radiation Protection and others, ICNIRP statement on the "guidelines for limiting exposure to time-varying electric, magnetic, and electromagnetic fields (up to 300 GHz)", Health Phys. 97 (3) (2009) 257–258.

[6] C. Chou, H. Bässen, J. Osepchuk, G. Balzano, R. Petersen, M. Meitz, R. Cleveland, J. Lin, L. Heynick, Radio frequency electromagnetic exposure, J. Bioelectromagn. 17 (1996) 195–208.
[7] T. Schmid, O. Egger, N. Kuster, Automated E-field scanning system for dosimetric assessments, IEEE Trans. Microw. Theory Tech. 44 (1) (1996) 105–113.
[8] Q. Balzano, O. Garay, T.J. Manning Jr., Electromagnetic energy exposure of simulated users of portable cellular telephones, IEEE Trans. Veh. Technol. 44 (3) (1995) 390–403.
[9] International Electrotechnical Commission and others, Human exposure to radio frequency fields from hand-held and body-mounted wireless communication devices–human models, instrumentation, and procedures, 2009.
[10] IEEE Recommended Practice for Determining the Peak Spatial-Average Specific Absorption Rate (SAR) in the Human Head from Wireless Communications Devices: Measurement Techniques, IEEE Std 1528-2003 (2003) 1–120, http://dx.doi.org/10.1109/IEEESTD.2003.94414.
[11] CENELEC EN50383, Basic standard for the calculation and measurement of electromagnetic field strength and SAR related to human exposure from radio base stations and fixed terminal stations for wireless telecommunication systems (110 MHz–40 GHz), Technical committee 211.
[12] IEEE Recommended Practice for Determining the Peak Spatial-Average Specific Absorption Rate (SAR) in the Human Head from Wireless Communications Devices: Measurement Techniques – Amendment 1: CAD File for Human Head Model (SAM Phantom), IEEE Std 1528a-2005 (Amendment to IEEE Std 1528-2003) (2006) 1–11, http://dx.doi.org/10.1109/IEEESTD.2006.99106.
[13] P. Glover, R. Bowtell, Measurement of electric fields due to time-varying magnetic field gradients using dipole probes, Phys. Med. Biol. 52 (17) (2007) 5119.
[14] C. Gottueb, M. Hagmann, T. Babü, A. Abitbol, A. Lewin, P. Houdek, J. Schwade, Interstitial microwave hyperthermia applicators having submillimetre diameters, Int. J. Hyperth. 6 (3) (1990) 707–714.
[15] C. Gabriel, S. Gabriel, E. Corthout, The dielectric properties of biological tissues: I. Literature survey, Phys. Med. Biol. 41 (11) (1996) 2231.
[16] S. Gabriel, R. Lau, C. Gabriel, The dielectric properties of biological tissues: II. Measurements in the frequency range 10 Hz to 20 GHz, Phys. Med. Biol. 41 (11) (1996) 2251.
[17] B.B. Beard, W. Kainz, T. Onishi, T. Iyama, S. Watanabe, O. Fujiwara, J. Wang, G. Bit-Babik, A. Faraone, J. Wiart, et al., Comparisons of computed mobile phone induced SAR in the SAM phantom to that in anatomically correct models of the human head, IEEE Trans. Electromagn. Compat. 48 (2) (2006) 397–407.
[18] J. Wiart, A. Hadjem, M. Wong, I. Bloch, Analysis of RF exposure in the head tissues of children and adults, Phys. Med. Biol. 53 (13) (2008) 3681.
[19] O.M. Bucci, C. Gennarelli, C. Savarese, Representation of electromagnetic fields over arbitrary surfaces by a finite and nonredundant number of samples, IEEE Trans. Antennas Propag. 46 (3) (1998) 351–359.
[20] O.M. Bucci, G. Franceschetti, On the spatial bandwidth of scattered fields, IEEE Trans. Antennas Propag. 35 (12) (1987) 1445–1455.
[21] O. Bucci, T. Isernia, Electromagnetic inverse scattering: retrievable information and measurement strategies, Radio Sci. 32 (6) (1997) 2123–2137.
[22] O.M. Bucci, L. Crocco, T. Isernia, V. Pascazio, Subsurface inverse scattering problems: quantifying, qualifying, and achieving the available information, IEEE Trans. Geosci. Remote Sens. 39 (11) (2001) 2527–2538.
[23] A. Hadjem, D. Lautru, C. Dale, M.F. Wong, V.F. Hanna, J. Wiart, Study of specific absorption rate (SAR) induced in two child head models and in adult heads using mobile phones, IEEE Trans. Microw. Theory Tech. 53 (1) (2005) 4–11.
[24] M.-F. Wong, J. Wiart, Modelling of electromagnetic wave interactions with the human body, C. R. Physique 6 (6) (2005) 585–594.
[25] E. Conil, A. Hadjem, F. Lacroux, M. Wong, J. Wiart, Variability analysis of SAR from 20 MHz to 2.4 GHz for different adult and child models using finite-difference time-domain, Phys. Med. Biol. 53 (6) (2008) 1511.
[26] G. Scarella, O. Clatz, S. Lanteri, G. Beaume, S. Oudot, J.-P. Pons, S. Piperno, P. Joly, J. Wiart, Realistic numerical modelling of human head tissue exposure to electromagnetic waves from cellular phones, C. R. Physique 7 (5) (2006) 501–508.
[27] M. Mashevich, D. Folkman, A. Kesar, A. Barbul, R. Korenstein, E. Jerby, L. Avivi, Exposure of human peripheral blood lymphocytes to electromagnetic fields associated with cellular phones leads to chromosomal instability, Bioelectromagnetics 24 (2) (2003) 82–90.
[28] J. Bakker, M. Paulides, E. Neufeld, A. Christ, X. Chen, N. Kuster, G. Van Rhoon, Children and adults exposed to low-frequency magnetic fields at the ICNIRP reference levels: theoretical assessment of the induced electric fields, Phys. Med. Biol. 57 (7) (2012) 1815.
[29] G. Lazzi, O.P. Gandhi, On modeling and personal dosimetry of cellular telephone helical antennas with the FDTD code, IEEE Trans. Antennas Propag. 46 (4) (1998) 525–530.
[30] Y. Liu, Z. Liang, Z. Yang, Computation of electromagnetic dosimetry for human body using parallel FDTD algorithm combined with interpolation technique, Prog. Electromagn. Res. 82 (2008) 95–107.
[31] F.J. Meyer, D.B. Davidson, U. Jakobus, M.A. Stuchly, Human exposure assessment in the near field of GSM base-station antennas using a hybrid finite element/method of moments technique, IEEE Trans. Biomed. Eng. 50 (2) (2003) 224–233.
[32] K.D. Paulsen, X. Jia, J.M. Sullivan Jr., Finite element computations of specific absorption rates in anatomically conforming full-body models for hyperthermia treatment analysis, IEEE Trans. Biomed. Eng. 40 (9) (1993) 933–945.
[33] J. Hand, Modelling the interaction of electromagnetic fields (10 MHz–10 GHz) with the human body: methods and applications, Phys. Med. Biol. 53 (16) (2008) R243.
[34] D. Lautru, J. Wiart, W. Tabbara, Calculation of the power deposited in a phantom close to a base station antenna using a hybrid FDTD-MOMTD approach, in: 30th European Microwave Conference, 2000, IEEE, 2000, pp. 1–4.
[35] Y. Pinto, A. Ghanmi, A. Hadjem, E. Conil, T. Namur, C. Person, J. Wiart, Numerical mobile phone models validated by SAR measurements, in: Proceedings of the 5th European Conference on Antennas and Propagation, EUCAP, 2011.
[36] J. Zhu, D. Jiao, A theoretically rigorous full-wave finite-element-based solution of Maxwell's equations from DC to high frequencies, IEEE Trans. Adv. Packaging 33 (4) (2010) 1043–1050.
[37] O. Bottauscio, M. Chiampi, L. Zilberti, A boundary element approach to relate surface fields with the specific absorption rate (SAR) induced in 3-D human phantoms, Eng. Anal. Bound. Elem. 35 (4) (2011) 657–666.
[38] O. Bottauscio, M. Chiampi, L. Zilberti, Boundary element approaches for the evaluation of human exposure to low frequency electromagnetic fields, IEEE Trans. Magn. 45 (3) (2009) 1674–1677.
[39] D. Giordano, L. Zilberti, M. Borsero, M. Chiampi, O. Bottauscio, Experimental validation of MRI dosimetric simulations in phantoms including metallic objects, IEEE Trans. Magn. 50 (11) (2014) 1–4.
[40] R. Albanese, P.B. Monk, The inverse source problem for Maxwell's equations, Inverse Probl. 22 (3) (2006) 1023.
[41] A. Lakhal, A. Louis, Locating radiating sources for Maxwell's equations using the approximate inverse, Inverse Probl. 24 (4) (2008) 045020.
[42] E.A. Marengo, A.J. Devaney, R.W. Ziolkowski, Inverse source problem and minimum-energy sources, J. Opt. Soc. Am. A 17 (1) (2000) 34–45.
[43] A.J. Devaney, E.A. Marengo, M. Li, Inverse source problem in nonhomogeneous background media, SIAM J. Appl. Math. 67 (5) (2007) 1353–1378.
[44] G. Gragnani, M.D. Mendez, Improved electromagnetic inverse scattering procedure using non-radiating sources and scattering support reconstruction, IET Microw. Antennas Propag. 5 (15) (2011) 1822–1829.
[45] J. Sylvester, Notions of support for far fields, Inverse Probl. 22 (4) (2006) 1273.
[46] A. Beck, M. Teboulle, A fast iterative shrinkage-thresholding algorithm for linear inverse problems, SIAM J. Imaging Sci. 2 (1) (2009) 183–202.
[47] S.C. Park, M.K. Park, M.G. Kang, Super-resolution image reconstruction: a technical overview, IEEE Signal Process. Mag. 20 (3) (2003) 21–36.
[48] I. Daubechies, M. Defrise, C. De Mol, An iterative thresholding algorithm for linear inverse problems with a sparsity constraint, arXiv:math/0307152.

[49] A. Abubakar, P. Van den Berg, S. Semenov, Two-and three-dimensional algorithms for microwave imaging and inverse scattering, J. Electromagn. Waves Appl. 17 (2) (2003) 209–231.
[50] T. Rubk, P.M. Meaney, P. Meincke, K.D. Paulsen, Nonlinear microwave imaging for breast-cancer screening using Gauss–Newton's method and the CGLS inversion algorithm, IEEE Trans. Antennas Propag. 55 (8) (2007) 2320–2331.
[51] P.M. Meaney, M.W. Fanning, D. Li, S.P. Poplack, K.D. Paulsen, A clinical prototype for active microwave imaging of the breast, IEEE Trans. Microw. Theory Tech. 48 (11) (2000) 1841–1853.
[52] J. De Zaeytijd, A. Franchois, C. Eyraud, J.-M. Geffrin, Full-wave three-dimensional microwave imaging with a regularized Gauss–Newton method—theory and experiment, IEEE Trans. Antennas Propag. 55 (11) (2007) 3279–3292.
[53] J. De Zaeytijd, A. Franchois, Three-dimensional quantitative microwave imaging from measured data with multiplicative smoothing and value picking regularization, Inverse Probl. 25 (2) (2009) 024004.
[54] K. Cools, F.P. Andriulli, E. Michielssen, A Calderón multiplicative preconditioner for the PMCHWT integral equation, IEEE Trans. Antennas Propag. 59 (12) (2011) 4579–4587.
[55] O.D. Kellogg, et al., Foundations of Potential Theory, New York, 1929.
[56] J.L.A. Quijano, G. Vecchi, Field and source equivalence in source reconstruction on 3D surfaces, Prog. Electromagn. Res. 103 (2010) 67–100.
[57] S.M. Rao, D. Wilton, A.W. Glisson, Electromagnetic scattering by surfaces of arbitrary shape, IEEE Trans. Antennas Propag. 30 (3) (1982) 409–418.
[58] D.H. Schaubert, D.R. Wilton, A.W. Glisson, A tetrahedral modeling method for electromagnetic scattering by arbitrarily shaped inhomogeneous dielectric bodies, IEEE Trans. Antennas Propag. 32 (1) (1984) 77–85.
[59] W.C. Chew, J.-M. Jin, E. Michielssen, J. Song, Fast and Efficient Algorithms in Computational Electromagnetics, ARTECH House, 2001.
[60] M. Leibfritz, F. Landstorfer, T. Eibert, An equivalent source method to determine complex excitation levels of antenna arrays from near-field measurements, in: The Second European Conference on Antennas and Propagation, 2007, EuCAP 2007, IET, 2007, pp. 1–7.
[61] F. Andriulli, A. Tabacco, G. Vecchi, Solving the EFIE at low frequencies with a conditioning that grows only logarithmically with the number of unknowns, 58 (5) (2010) 1614–1624, http://dx.doi.org/10.1109/TAP.2010.2044325.
[62] F. Andriulli, Loop-star and loop-tree decompositions: analysis and efficient algorithms, 60 (5) (2012) 2347–2356, http://dx.doi.org/10.1109/TAP.2012.2189723.
[63] F. Andriulli, K. Cools, I. Bogaert, E. Michielssen, On a well-conditioned electric field integral operator for multiply connected geometries, IEEE Trans. Antennas Propag. 61 (4) (2013) 2077–2087.
[64] F.P. Andriulli, K. Cools, H. Bagci, F. Olyslager, A. Buffa, S. Christiansen, E. Michielssen, A multiplicative Calderón preconditioner for the electric field integral equation, 56 (8) (2008) 2398–2412.
[65] J.-C. Nedéléc, Acoustic and Electromagnetic Equations, Springer, 2000.
[66] A. Buffa, S.H. Christiansen, A dual finite element complex on the barycentric refinement, Math. Comput. 76 (260) (2007) 1743–1769.